Earth and Planetary Science Letters
January 2017, Volume 458, Pages 366-379
http://dx.doi.org/10.1016/j.epsl.2016.11.004
http://archimer.ifremer.fr/doc/00358/46957/

Glacial erosion dynamics in a small mountainous watershed (Southern French Alps): A source-to-sink approach

Bonneau Lucile [1, 2, *], Toucanne Samuel [2], Bayon Germain [2], Jorry Stéphan [2], Emmanuel Laurent [1], Silva Jacinto Ricardo [2]

[1] Université Pierre et Marie Curie, Laboratoire Biominéralisations et Environnements Sédimentaires, ISTeP–UMR CNRS 7193, 75252 Paris, France
[2] IFREMER, Unité de Recherche Géosciences Marines, Laboratoire Géophysique et Enregistrements Sédimentaires, F-29280 Plouzané, France

* Corresponding author : Lucile Bonneau, email address : lbonneau@iup.uni-heidelberg.de

Abstract :

In this study we used major element composition, neodymium isotopes ratios (εNdεNd) and concentration of REE to track and quantify the sediment routing in the Var sedimentary system from source (Southern French Alps) to sink (Ligurian Sea) over the last 50 ka. Our data reveal that changes in sediment sources over that period, associated with concomitant changes in the hyperpycnal (i.e. flood-generated turbidity currents) activity in the Var submarine canyon, were mainly driven by paleoenvironmental conditions in the upper basin and in particular by the presence of glaciers during the last glacial period. Based on this evidence, we determined when and how glacier-derived sediments were produced, then excavated and transferred to the ocean, allowing us to ultimately tune offshore sedimentary records to onshore denudation rates. In contrast to large glaciated systems, we found that sediment export from the Var River to the Mediterranean Sea directly responded to climate-induced perturbations within the basin. Finally, we estimated that sediment fluxes in the Var routing system were 2.5 times higher during the Last Glacial Maximum than today, thus confirming that glacier denudation rates exceed fluvial rates and that such a pattern also governs the interglacial–glacial sediment flux cycle in other small mountainous basins

Highlights

► We used εNdεNd to track the sediment routing in the Var system over the last 50 kyr. ► Glaciers are the main driver of the glacial/interglacial cycle of sediment flux. ► The estimated sediment fluxes are 2.5 times higher during the LGM than today. ► A major change in turbidite activity and sources is observed between 19 and 16 ka. ► The glacial sediment transfer to the sea depends on the catchment's characteristics.

Keywords : Var, routing system, glacial erosion, source-to-sink

1. Introduction

Weathering processes and their evolution through time are intensely debated, especially in active mountain belts where tectonic and climate forcings are well expressed at the geological timescale (Molnar, 2004; Koppes and Montgomery, 2009; Willenbring et al., 2013). Glaciers constitute a prominent phenomenon in such environments since they induce high denudation rates, especially in temperate settings (Hallet et al., 1996; Koppes and Montgomery, 2009; Koppes et al., 2015). Nevertheless, the relevance of mountains in the relationship between tectonic, climate and weathering has been recently questioned since variations in denudation rate in highlands over glacial-interglacial cycles could have been counterbalanced by opposite changes in lowlands (Willenbring et al., 2013; Hidy et al., 2014). Many studies attempt to correlate sediment yield/denudation rates and glacier/climate parameters by analyzing global dataset (Koppes and Montgomery 2009; Willenbring et al., 2013; Koppes et al., 2015) but only a few have addressed this issue by focusing on the temporal variations, at high-resolution, of sediment flux from a single sedimentary system (e.g. Elverhoi et al., 1998; Calvès et al., 2012). As a result, and despite the recent development of conceptual models (Hinderer, 2012; Romans et al., 2015; Jaeger and Koppes, 2016) and numerical simulations (Castelltort and Van Den Driessche, 2003; Simpson and Castelltort, 2012), our understanding remains limited. Many glaciated catchments show a substantial decrease in sediment yield at glacial-interglacial transitions (e.g., in Asia : Clift et al., 2008; Clift and Giosan, 2014; in the European Alps: Hinderer, 2001, Savi et al., 2014; or in small Mediterranean catchments : Woodward et al., 1992, 2008; Adamson et al., 2014) while it is accepted that the ability of rivers to transmit high glacier-derived sediment yield to the sea under glacial arid climate is low (Hinderer, 2001, 2012). As a result, it appears crucial to determine when and how glacier-derived sediments are produced, then excavated and transferred to the ocean, in order to ultimately link offshore sedimentary records to onshore denudation rates. The absence of a large floodplain and of a continental shelf in the mountainous Var sediment routing system (Southern French Alps), usually known to buffer the seaward propagation of the landscape response to tectonic and climate forcings (e.g. Milliman and Syvitski, 1992; Covault et al., 2013), makes this system a rare and ideal target to focus on this topic at high-resolution. The substantial impact of the growth and decay of the Alpine Ice-Sheet, as well as of the Dansgaard-Oeschger (D/O) millennial-scale climate oscillations, on sediment transfer in the last glacial Var sediment routing system strongly support this assumption (Jorry et al., 2011; Bonneau et al., 2014).

In this study, major/trace element concentrations, and neodymium isotopic ratios (εNd) have been determined in sediments from the Var River basin and its offshore turbidite system, for the last 50 kyr. The combined analysis of terrestrial sources and turbidite activity allows us to provide constraints on the glacial - deglacial pattern of sediment yield associated with a small glaciated basin. When compared to case studies from other larger sediment routing systems, this study brings new insights into how transfer-lag can introduce a bias on the source-to-sink approach at glacial-interglacial time-scale.

2. Regional setting

The Var River (SE France) and its main tributaries (Tinée, Vésubie, Esteron and Cian rivers) drain a total area of 2800 km², from the Southern French Alps to the Ligurian Sea (Western Mediterranean). No hydropower dams are present in the catchment area. The Var drainage area is characterized by a steep slope (mean 23°) and a mean/maximum altitude of ca. 1200 m and 3200 m, respectively. Typical hillslope erosional processes of steep mountainous and formerly glaciated catchments (gullies, landslides, etc) are observed all over the basin (Julian, 1977). The Var drainage area is mainly composed of Mesozoic carbonate rocks (mainly limestones and marls) locally covered by Cenozoic sandstones, marls and limestones (Kerckhove et al., 1979; Rouire et al., 1980; Fig. 1). Paleozoic External Crystalline Massifs form the upper reaches in the eastern part of the drainage area (Mercantour Massif). They are composed of occidental (Tinée, TMC) and oriental (Malinvern-Argentera, OMC) metamorphic complexes that outcrop in the NE part of the Tinée sub-basin and in the upper Vésubie sub-basin, respectively, and of the Argentera granite. Locally, Permian pelites are found in unconformity on the edge of the External Crystalline Massifs and in the central part of the drainage area. The lower Var valley corresponds to the filling of the Messinian Var valley during Plio-Quaternary, and is now occupied by a braided gravely channel bordered by steep hillslopes. The Var delta, that is very limited in extent (5 km²), is built on the edge of the narrow (virtually absent off the river mouth) continental shelf (Piper and Savoye 1993). The modern sediment yield is estimated at 1.63 Mt/yr, i.e. a specific sediment flux of 580 t/km²/yr (Mulder et al., 1997, 1998). The discharge of the Var River is characterized by a significant seasonality. High water discharges occur during spring when snow melts, and during autumn when rainfall is high. Heavy rainfall can produce floods, with peak discharges of the Var River exceeding 1000 m^3/s, i.e. 20 times the mean annual discharge (50 m^3/s).

The Var River mouth is directly connected to the head of a submarine canyon. The Var canyon joins the Paillon canyon to form a single valley that feeds a channel-levee system (Var Sedimentary Ridge, VSR) ended by a distal lobe which extends to the continental slope of Corsica Island (Fig. 1). Turbidites on the VSR originate from the overflow of (i) turbidity currents that follow a large (earthquake-related) mass wasting initiated at the top of the continental slope in unconsolidated sediments (Mulder et al., 1998; Migeon et al., 2011), and (ii) hyperpycnal currents triggered during high magnitude floods of the Var River (Piper and Savoye 1993; Mulder et al., 1997, 1998). All the characteristics described above make the Var sedimentary system a potential reactive system (Covault et al., 2013) and a unique target to investigate forcings on sediment flux. Recently, a climate-related pattern has been highlighted in the feeding of the offshore part of the Var sediment routing system over the last 75 kyr (Jorry et al., 2011; Bonneau et al., 2014) through the direct correlation between the turbidite activity on the VSR and climate conditions in the Var catchment at the scale of both glacial-interglacial and D/O cycles. Such a direct connection between climate and deep-sea sedimentation is likely to be carried by hyperpycnal activity of Var river floods that is highly dependent of the balance between water discharge and sediment load (Mulder and Syvitski, 1995; Mulder et al., 1997, 1998). High hyperpycnal activity observed during the last glacial seems mainly to have been caused by the presence of glaciers in the Var valleys and high sediment-concentrated glacial outwash (Piper and Savoye, 1993; Bonneau et al., 2014). We discuss this assumption below.

3. Material and Methods

3.1. Sampling method

Chemical analyses were performed on the <63 µm fraction of both marine and riverine sediments. This grain-size fraction encompasses that of marine sediments deposited on the

VSR (Savoye et al., 1993), as well as that of the suspended sediment load of the Var River (Gennesseaux, 1966). Some marine (n=9) and riverine (n=7) samples were separated into the 0-45 µm and 45-63 µm grain-size fractions in order to test the possibility of a relationship between grain size and sediment sources.

3.2. Sampling method in the Var River watershed

A total of 43 sediment samples were collected on the river bed of the Var River and its tributaries, in order to determine the geochemical signature of the main lithological units and to quantify the sedimentary mixing that may occur along the onshore sediment route. Because fine-grained sediments (<63µm) in the river bed are generally not abundant because of winnowing during floods, sheltered areas (i.e. low-energy meanders, base of boulders) have preferentially been sampled. Bulk sediments were passed through a 63-µm sieve on site to obtain several tens of grams of fine sediments. Each sample is regarded as representative of sediments delivered by the upstream drained area.

3.3. Sampling method in sediment cores

We studied two cores collected during the ESSDIV cruise (2008) onboard the R/V *Pourquoi pas?* : a 22 meter-long core recovered on the top of the middle VSR (ESSK08-CS01), and a 24 meter-long core recovered on the southern VSR (ESSK08-CS13). The sediments consist of alternations of millimeter to decimeter-scale turbiditic sandy/silty sequences and hemipelagic muds. The chronostratigraphic framework is well-constrained, and based on ^{14}C-AMS dates and the tuning of the planktic foraminifera *Globigerina bulloides* $\delta^{18}O$ record to the NGRIP record (see Jorry et al., 2011; Bonneau et al., 2014 for details).

For this study, the upper part (i.e. silty-clay size fraction) of 91 turbidite sequences in core ESSK08-CS01 (n=53; between 0 -30 kyr BP) and core ESSK08-CS13 (n=38; between

30-50 kyr BP) were sampled in order to obtain a mean resolution of ca. 500 yr on the studied time period.

3.4. Analytical methods

3.4.1. Major and minor element composition

Major element concentrations were measured in selected riverine (n=21) and marine (n=11) samples. The chemical composition of bulk sediment samples was determined by wavelength-dispersive X-ray fluorescence (WD-XRF) using a Siemens SRS 303 sequential X-ray spectrometer (IFREMER, Brest, France). Analyses were performed on fusion beads prepared with 500 mg of sediment. Major element concentrations are expressed in weight % oxides (SiO_2, Al_2O_3, Fe_2O_3, MnO, CaO, MgO, K_2O, Na_2O, TiO_2, P_2O_5, SO_4). Minor element concentrations are expressed in ppm (V, Cr, Co, Ni, Cu, Zn, Sr, Zr, Ba). The measurement precision is between 0.01% and 0.2% for major elements and several ppm for minor elements.

3.4.2. Neodymium isotopic composition and REE concentration

Rare earth element (REE) abundances and neodymium isotopic compositions ($^{143}Nd/^{144}Nd$ ratios) were determined on each sample. Prior to Nd isotopic and REE measurements, about 700 mg of sediment were leached sequentially in order to remove any carbonate, Fe-Mn oxyhydroxides and organic compounds (Bayon et al., 2002). The resulting residual sediment is referred to as the carbonate-free fraction in the following text. Then, about 100 mg of sediment were digested by alkaline fusion after addition of a Tm spike (Bayon et al, 2009). REE concentrations were determined by ICPMS (Quad X Series 2 and ELEMENT 2) at the Pôle Spectrométrie Océan (PSO, Brest, France). The precision of analysis is better than 5%.

Nd was purified by ion-exchange chromatography, and Nd isotopic ratios were measured by MC-ICP-MS (Neptune, PSO). Nd isotopic compositions are expressed using the epsilon notation, which corresponds to the deviation of measured $^{143}Nd/^{144}Nd$ ratios relative to a chondritic uniform reservoir (CHUR) value of 0.512638 (Jacobsen and Wasserburg, 1980). During the course of this study, replicate analyses of JNdi (n = 80) and La Jolla (n = 10) standard solutions gave mean $^{143}Nd/^{144}Nd$ values of 0.512115 ± 0.000009 (εNd = -10.16 ± 0.18; 2 sd) and 0.511862 ± 0.000011 (εNd = -15.10 ±0.21 ; 2 sd), respectively; hence corresponding to an estimated external reproducibility of about 0.2 epsilon units. Note that the in-run errors (2se) associated to sample analyses were systematically lower.

4. Results

4.1. Major element composition

4.1.1. Chemical composition of the river sediments

The river samples can be divided into two groups on the basis of their chemical composition (Table 1; Fig. 2):

- Samples collected in the Vésubie and NE Tinée drainage basins are characterized by low contents of CaO (< 6%), Sr (< 250 ppm) and LOI (< 10%), and high contents of Al_2O_3 (13-20%), SiO_2 (> 50%), K_2O (3-5%), and NaO (1.5-3%) and, to a lesser extent, high contents of TiO_2, MgO and Zr. Their chemical composition is consistent with the fact that these sediments are mainly derived from the erosion of the External Crystalline Massifs;
- Samples derived from the erosion of carbonate-rich sedimentary formations are characterized by high contents of CaO (> 20%), Sr (> 500 ppm) and LOI (20-30%),

low contents of Al_2O_3 (4.5-10%), SiO_2 (25-45%), K_2O (<2%), and NaO (<1%) and by relatively low contents of TiO_2, MgO, Zr..

The chemical composition of sediments sampled near the Var river mouth is indistinguishable from that of the second group of samples. This indicates that sedimentary formations that cover 84% of the total drainage area (16% for External Crystalline Massifs) are the main contributor of the sediment load exported from the Var watershed.

4.1.2 Chemical composition of the marine sediments

A significant change in the chemical composition (i.e. a decrease of detrital element abundances; Si, Al, K, Fe, Ti, Rb) of the VSR sediments at ca. 16 ka was reported by Bonneau et al. (2014) on the basis of semi-quantitative geochemical profiling with an X-ray fluorescence (XRF) core scanner. The major element concentrations of 10 samples of turbidite sediments (ESSK08-CS01) dated from 19 to 15 ka, were quantified by wavelength-dispersive XRF spectrometry in order to check if this signal is carried by turbidites and therefore reflects a change in the source of sediments.

Chemical compositions of turbidite sediments are plotted in Fig. 2 on Harker diagrams with the river samples. Between 19 and 15 ka, the concentrations (wt. %) of siliciclastic elements decrease from 40% to 33% of SiO_2, from 11% to 8% of Al_2O_3 and from 2.3% to 1.3 % of K_2O, while the concentration in CaO increases from 18 % to 25% (Fig. 2). The most recent sample (ca. 15 ka) has a chemical composition similar to that of the modern sediment sampled at the Var River mouth. The composition of glacial (from 20 to 17 ka) samples is intermediate between samples from sedimentary formations (blue symbols in Fig. 2) and sediments from External Crystalline Massifs (red symbols in Fig. 2). A siliciclastic index $(Al_2O_3+K_2O+MgO+NaO+Fe_2O_3+Ti_2O)$ / $(CaO+SiO_2+Al_2O_3+K_2O+MgO+NaO+Fe_2O_3+Ti_2O)$ was calculated for each sample.

4.2. Neodymium isotopic composition

4.2.1. River sediments

The studied river sediment samples display εNd values ranging from -11.5 to -7.9 (Fig. 3, refer to Supplementary material for details), with sediments derived from the External Crystalline Massifs exhibiting slightly more radiogenic values (-10.7 < εNd < -7.8) than those originating from sedimentary formations (-11.5 < εNd < -10.0; mean= -11.3). Sediments sampled in the Vésubie sub-basin exhibit a Nd isotopic composition very different from the basin-wide signature (-9.3 < εNd < -7.8; mean = -8.2). This signature can be attributed to the presence of the Oriental metamorphic complex (OMC) that outcrops in the Vésubie sub-basin. A similar εNd value (-8.7) is obtained for a sample from the Nègre Lake that drains the Argentera granite. The sediments delivered by the third part of the External Crystalline Massifs, the Tinée metamorphic complex (TMC), exhibit a εNd value around -10.7 as found in the lower Var Valley (-10.9 < εNd < -10.4).

4.2.2. Marine sediments

εNd values in the turbidite sediments (-10.9 < εNd < -9.6; Fig. 3, 4) are within the range of values obtained for the Var watershed (-11.5 < εNd < -7.8; Fig. 3a, b). The youngest sample (dated at ca.1.5 ka; Bonneau et al., 2014), exhibits an εNd value (-10.4), similar to those measured near the modern river mouth (-10.9 < εNd < -10.4). εNd values obtained for the last glacial period are more radiogenic (50-19 ka; -9.6 < εNd < -10.4, mean = -10.1; n=59) than those obtained for the Late Glacial and the Holocene (16-0 ka; -10.4 < εNd < -10.9, mean = -10.6; n=32) except between 11 and 9 ka when a reversal toward more radiogenic composition is observed (εNd up to -10 at 10 ka). The transition in the εNd between full glacial and Late Glacial conditions occurred between 19 and 16 ka, and is defined by a shift (about -0.6 in εNd) to less radiogenic Nd composition.

4.3. REE abundance

REE concentrations normalized to Post-Archean average Australian Shale (PAAS; Taylor and McLennan, 1985) are reported in Fig. 3.c. The mid-REE-depleted pattern of sediments from the lower Var valley slightly differs from the typical REE signatures of world river clays (Bayon et al., 2015). REE pattern analysis at a sub-basin scale reveals that this particular mid-REE depletion is likely carried by Permian pelites – an important source of clay-size sediments – outcropping in the upper Var valley (Fig. 3.c.). High REE concentrations found in sediments from the Vésubie and Upper Tinée sub-catchments that erode the External Crystalline Massifs are probably related to the presence of REE-rich accessory minerals, as highlighted by the enrichment in HREE.

In comparison to modern sediments collected in the downstream part of the Var River, marine sediments are depleted in REE (Fig. 3.c). This can reflect a loss of accessory minerals during sediment transport or a change in the phase bearing the REE. Marchandise et al. (2014) estimated that 20% of the REE in the Var sediments are transported in insoluble accessory minerals, the remainder being distributed in other phases (clay, organic matter or Fe/Mn oxyhydroxide). Mineral density-related sorting caused by hydrodynamic processes can occur in river channels (Bouchez et al. 2011) or during submarine transport (e.g. Carpentier et al. 2014). In this context, turbulent flows that transport sediments onto the VSR could also play a role in depletion of REE-rich minerals in turbidites.

The depletion in mid-REE (e.g. Gd/Nd ratios increase) is slightly better expressed in interglacial sediments than in glacial sediment, which is consistent with the changes observed in Nd isotope ratios (εNd) and major elements composition.

5. Significance of εNd measured in marine sediments

5.1. *Gauging the grain size effect on εNd*

Recent studies have shown that different grain size fractions, due to hydrodynamic sorting of minerals, could derive from distinct sediment sources (Bouchez et al. 2011, Carpentier et al. 2014) associated with different transfer times (Clift and Giosan, 2014). In addition, grain-size dependent Nd isotopic signatures in river sediments can also reflect differences in lithological sensitivity to weathering/erosion processes (Bayon et al., 2015). Taken together, these effects could induce a bias for source tracking, if grain size distribution differs from one sample to another.

In order to gauge this effect in the Var watershed, selected riverine and marine samples (dated from 20 to 0 ka) have been divided into two grain-size fractions (0-45µm and 45-63µm) and analyzed for Nd isotopes and REE concentrations (Table 2). In all samples, except for Vésubie sediments in which high Nd concentrations are found in both fractions, the concentration of Nd is higher in the 0-45 µm fraction. This suggests, in agreement with the recent results of Marchandise et al. (2014), that the Nd-bearing minerals in the Var sediments are preferentially incorporated in the fine fraction.

The εNd values measured in the two fractions are similar (< 0.2ε) except for some river sediments where more than one lithological unit is drained upstream of the sampling site (Table 2). Values obtained in the finest fraction (0-45 µm) are very similar to those obtained from the bulk (0-63 µm), being mainly composed of grains finer than 45 µm. In marine samples as well as at the Var River mouth, εNd values are more radiogenic in the 45-63µm fraction, showing that coarse particles are preferentially derived from Oriental Metamorphic Complex/ Vésubie River (Table 2). The downcore variability of εNd is the same in both grain size fractions (45-63 µm and 0-45 µm), with a more radiogenic εNd signature during glacial time (20-18 ka) and at around 10 ka. Importantly, this shows that changes in sediment sources affected each grain size fraction of the sediment. Additionally, grain size distribution of each turbidite sample (0-63 µm fraction) was systematically measured and compared with εNd values. No relationship is found between these two factors, showing that εNd values measured in <63 µm marine samples are not significantly influenced by grain size distribution but seem to reflect the terrestrial source of sediments.

5.2 Quantification of the terrestrial sources contribution in VSR sediments

When combining measured values for Nd isotopes (εNd) and concentrations in river samples, a distinctive signature can be assigned to sediments derived from the erosion of the three main lithological units found in the Var drainage area (Fig. 3.a; Table 3). In the following discussion, we postulate that variations in the measured εNd values of VSR sediments reflect changes in the mixing of the three end-member terrestrial sources in the sediment budget delivered by the Var River.

First, based on the fingerprint characteristics of these three end-members, two binary isotopic mixing curves between each Metamorphic Complexes and the sedimentary formations were constructed and plotted in a εNd vs Nd concentration diagram (Fig. 3.a). For a given mixing (*m*) between two end-members *a* and *b* Nd isotope ratio and Nd concentration are:

$$[Nd]_{(m)} = [Nd]_{(a)} \times F + [Nd]_{(b)} \times (1 - F)$$

$$\frac{^{143}Nd}{^{144}Nd}(m) = \frac{^{143}Nd}{^{144}Nd}(a)\frac{[Nd]_{(a)}}{[Nd]_{(m)}}F + \frac{^{143}Nd}{^{144}Nd}(b)\frac{[Nd]_{(b)}}{[Nd]_{(m)}}(1 - F)$$

where *F* is the proportion of *a* in the mixing : $F = \frac{a}{a + b}$.

The samples collected in the Tinée and Vésubie sub-basins fit along the sedimentary cover –TMC and –OMC mixing curves, respectively. In contrast, samples from the Var lower valley, derived from the mixing between the three end-members, are positioned between the two curves (Fig. 3.a). Nevertheless, their position, closer to the sedimentary cover end-member shows that even in the carbonate-free fraction the sedimentary cover is the dominant source of the sediment at basin scale. The two Metamorphic Complexes have similar geological (lithology), geographical (altitude, slope, latitude) and geomorphological (presence of glaciers during the LGM period) characteristics and can also be considered to be subject to similar erosion in terms of magnitude and processes (Syvitski and Milliman, 2007). As a result, in a proportion relative to their outcrop areas (Table 3), the two Metamorphic Complexes should similarly contribute to the mixing of sediments. Taking this into account, it is possible to balance a mixing model between the three end-members and therefore to predict the relative contribution of each one for a given εNd value measured in VSR sediment (i.e. for a given εNd, a single result may satisfy the proportional relationship between the two Metamorphic Complex).

When compared to values obtained for the Holocene and Late Glacial (-10.8 < εNd < -10.5), εNd values as radiogenic as -10.0 in glacial turbidites reflect a higher contribution of the Oriental Metamorphic Complex (i.e. Vésubie River). As Nd concentrations in VSR sediments (about 20 - 25 ppm) do not significantly vary because of the loss in Nd during the sediment transfer by depletion of Nd-rich minerals (Marchandise et al., 2014), the scatter of samples in Fig.3.a along the εNd axis most likely essentially reflects changes in the contribution of sediment sources from the Oriental Metamorphic Complex relative to the other sectors of the drainage area (mixing curves *a* and *b* in Fig.3.b). The composition of sediment derived from the rest of drainage area (mixing curve *c* in Fig.3.b) has a low impact on the εNd value of the mixing. In the mixing model, we assigned a fixed Nd concentration of 30 ppm to the two Metamorphic Complexes end-members, assumed to represent a more reliable estimate for the fraction of sediment exported to the studied site (hence taking into account the presumed loss of REE-bearing accessory minerals during sediment transport and hydrodynamic processes) (Fig. 3.b). To test the validity of this assumption, two additional mixing models were investigated: one using the actual concentration of end-members (results are shown between brackets in Table 4) and a εNd-Gd/Nd mixing model, which both gave results very similar to the concentration-adjusted Nd-εNd model presented thereafter.

Based on the above, measured εNd values could be converted into corresponding percentage proportions of the OMC end-member in the sediment (Fig. 4.c). We found that the total variability of εNd (1.3 εNd units) reflects a change of 40% in the proportion of OMC-derived sediments in the mixing (Fig. 3.b; Fig. 4.c). By using a mean εNd value of sediments during the Holocene (9-0 ka; -10.6) and the LGM (26-19 ka; -10.0), the proportion of OMC, TMC and sedimentary formations in the carbonate-free fraction of sediment are estimated respectively at 13 %, 17% and 70% for the Holocene and 29%, 39% and 32% for the LGM (Fig. 3.b, Table 4). As these results were obtained on the carbonate-free fraction of the sediment, inputs from External Crystalline Massifs have more weight in the mixing. To report proportions of bulk sediment, the carbonate-free fraction was calculated using the difference in weight of the samples before and after leach operations (Table 4). The proportion of OMC, TMC and sedimentary formations in bulk sediments are respectively 7 %, 9% and 84% for the Holocene and 17 %, 23% and 60% for the LGM (Table 4).

Our results show that small variations in εNd can actually reflect large changes in source mixing. A thorough analysis of all components of the Nd budget (i.e. sources signature, Nd concentration, grain-size effect, etc.) thus appears essential to interpret εNd variations for source-to-sink approach.

6. Discussion

6.1. Imprint of glaciers on sediment transfers: A source-to-sink approach

When interpreted as a source proxy, major element compositions are consistent with εNd signature of turbidites (siliciclastic index and εNd are well correlated: $r^2 = 0.71$; Fig. 2). High siliciclastic element concentration associated with radiogenic εNd (around -10) during the last glacial (50-19 ka) indicates a larger sediment input from the External Crystalline Massifs than during the Holocene and the Late Glacial (16-0 ka; Fig. 4). This change in sediment provenance, characterized by a decrease in siliciclastic elements and a shift toward less radiogenic εNd, occurred between 19 and 16 ka. These new data strongly corroborate the change in the chemical composition of the VSR sediments previously reported by Bonneau et al. (2014) on the basis of semi-quantitative XRF geochemical profiling. Based on our isotopic mixing model, we estimate that during the LGM, the contribution of the External Crystalline Massifs (OMC and TMC) was 2.5 times higher than during the Holocene (Table 4). Two glaciers occupied the upper Tinée and Vésubie valleys during this period, and the External Crystalline Massifs were largely covered by ice (Fig. 1, Soutadé et al., 1987; Buoncristiani and Campy, 2004). Thus, we argue that the change of sediment provenance observed at our study site arises from the presence of these glaciers, the latter generating an average denudation rate / sediment yield in the External Crystalline Massifs higher than in the rest of the Var drainage area.

εNd of turbidites indicates that the contribution of the External Crystalline Massifs, where glaciers were located, was higher during glaciation and decreased synchronously with turbidite frequency after the LGM, between 19 and 16 ka (Bonneau et al., 2014, Fig. 4). This concomitant change in both the geochemical composition of the turbidites and their deposition frequency on the VSR indicates that changes occurring in the Var watershed have forced deep-sea sedimentation, suggesting that changes of both sediment source and turbidite activity are driven by the same process. High turbidite activity in the Var sedimentary system during the last glacial (50-19 ka) has been interpreted as the result of frequent hyperpycnal flows of high sediment-concentrated Var floods because of glaciofluvial outwash (increasing the sediment availability) and meltwater floods (Piper and Savoye, 1993; Bonneau et al., 2014). Considering our regional reconstruction (i.e. probability distributions) for the LGM maximum advance of glaciers (see Fig. 4 for details), we assume that both erosion and sediment transfer in the Var sediment routing system were strongly forced by the ice-masses during the last glacial and the LGM (i.e. until ca. 19 ka). This indicates that sediment transfer was highly efficient (i.e. short) during the last glacial period.

Based on this evidence, and because only a few ages (e.g. ^{10}Be dates) have been determined for moraine deposits onland (Bigot-Cormier et al., 2005; Darnault et al., 2012), we hypothesize that the glacier evolution in the Var watershed can be accurately reconstructed from the deep offshore sequences. The comparison of our dataset with probability distributions for alpine glacier fluctuations indicates that maxima in both the εNd (i.e. External Massif source) and the turbidite activity observed at ca. 26-24 ka and 22-20 ka in the Var sediment routing system are coeval with the early-LGM and LGM maximum ice-advances observed in the European Alps (e.g. Monegato et al., 2007). Similarly, the post-LGM glacier withdrawal occurring at the scale of the Alpine Ice-Sheet between 19 and 16 ka (centered at 17.5 ka; Fig. 4.e) is coeval with the decrease in both the contribution of the External Crystalline Massifs and the turbidite activity in the Var sediment routing system. Taken together, this indicates that the glacier extent, as well as the erosion in the upper Var watershed, substantially decreased between 19 and 16 ka (ie. during Heinrich Stadial 1). This is supported through the only age obtained in the Var catchment for post-LGM glacier retreat (18.2 ± 4.3 ^{10}Be ka, 1600 m a.s.l., Bigot-Cormier et al., 2005). After this episode, alpine glaciers have lost about 80% of their LGM volume, according to Ivy-Ochs et al. (2008). After 16 ka, turbidite activity remains low and less radiogenic εNd (around -10.6) indicates a lower contribution of the External Crystalline Massifs (16%). A significant exception exists between

11 and 8 ka, when a radiogenic excursion of Nd isotopes occurs to similar values as observed during the LGM (-10). This event, which came with a slight increase in turbidite activity, attests to an increase in sediment yield from (formerly)-glaciated areas (Fig. 4). This episode could be assigned to the Egesen-Kartell stadial, identified between 11.4 ka and 10.9 ka in the Southern Alps (Darnaud et al., 2012; Bigot-Cormier et al., 2005; Fig. 4.e). Nevertheless, at that time, the ELA (Equilibrium-Line Altitude) was about 1000 m higher than during LGM (Cossart et al., 2012; Federici et al., 2016) and, though small glaciers could have persisted during the Early Holocene at high-altitude in confined places (youngest ice retreat age reported in the watershed is 8.4 ± 0.94 ^{10}Be ka, 2700 m a.s.l., Darnault et al., 2012), they would unlikely have resulted in a drastic change in sediment source. Instead, we propose that this Early Holocene increase of sediment yield from formerly glaciated upper valleys to be a paraglacial reworking stage. The latter was likely triggered by the interplay of increase in rainfall - while interglacial vegetation was not yet fully developed at altitude (Vescovi et al., 2007)- and delayed landscape adaptation to deglaciation (e.g. triggering massive landslides dated at 10.3±0.5 ka, Bigot-Cormier et al., 2005). Interestingly, the increase in glacial-reworked sediment yield in upper Vésubie could have fostered the concomitant decrease in the Vésubie incision rate observed after 11 ka (Saillard et al., 2014; Fig. 4.b).

Compared to the detailed history of alpine glaciers depicted for the last deglaciation little is known before the LGM, especially during MIS3 (see Ivy-Ochs et al., 2008; Hughes and Woodward, 2009). The presence of glaciers in the Var catchment at that time has not yet been attested, but our data (i.e. the high contribution of External Crystalline Massifs sediment associated with high turbidite activity between 50 and 19 ka) suggest that glaciers were present as early as 50 ka in significant extent (Fig. 4). If εNd can be used as a glacier-size proxy, the extent of MIS3 glaciers in the Var basin might have been larger than during Lateglacial stages (16-11 ka; Gschnitz and Egesen stadials; Fig. 4). Fast but low-amplitude changes in the εNd source record during MIS3 relative to MIS2 (Fig. 4) could indicate that glaciers were unstable at that time, probably in response to D/O swings. Nevertheless, the variability in hyperpycnal activity recorded during D/O oscillations is not observed in the εNd source record (Fig. 4). Therefore, we propose that the main driving mechanism of hyperpycnal activity variability is not restricted to the upper watershed, but likely impacts the whole Var basin. This could be due to changes in the precipitation regime and the associated response of the vegetation cover (Sanchez-Goni et al., 2002). Nevertheless, the presence of glaciers during MIS3 could have fostered the sensitivity of hyperpycnal activity to environmental changes, since such changes in the εNd source record are not observed during D/O-like Late Glacial climate oscillations (e.g. Bølling-Allerød and Younger Dryas). These oscillations could be correlated with Mediterranean fluvial sequences observed in glaciated and non-glaciated catchments over the last glacial cycle (see Macklin et al., 2002 for a review).

6.2. Sediment yield and denudation rate of External Crystalline Massifs: the impact of glaciation.

Based on our calculations, the contribution of the External Crystalline Massifs (OMC and TMC) during the Holocene is estimated at 16% (Table 4) while sedimentary formations contribute to 84% of the total sediment flux. These proportions match exactly with percentages of drainage area covered by these two lithological units (Table 3). This implies that 'interglacial' erosion rates were equivalent in the External Crystalline Massifs and the sedimentary formations, and thus at the scale of the whole basin. Based on modern sediment flux for the Var River (1.64 Mt/yr; Mulder et al., 1997) – and using a density of 2.65 for sediment – we can estimate that the modern average denudation rate in the Var catchment is about 0.22 mm/yr. Considering the mean slope of the studied drainage area (23°), this rate is at the upper end of the range of erosion rates observed worldwide (Willenbring et al., 2013).

Our estimates for the last glacial suggest that the sediment provenance is about 40% for the External Crystalline Massifs (OMC and TMC) and about 60% for the lowland sedimentary formations. Considering the lithological outcrop area, this reveals that denudation rates were higher in the External Crystalline Massifs than in the rest of the drainage area during the last glacial. Erosion rates by LGM-glaciers in the External Crystalline Massifs have been estimated at 1.8 mm/yr by Darnault et al. (2012), in agreement with rates measured on glaciers located in similar lithological and tectonic settings (Hallet et al., 1996). This glacial rate is 8 times higher than our estimation of the modern erosion rate (0.22 mm/ yr). A similar difference between LGM and modern erosion rates has been estimated for the European Alps by Hinderer (2001, Fig. 5).

By using an erosion rate of 1.8 mm/yr for glaciers in the External Crystalline Massifs (Darnault et al., 2012) to constrain LGM sediment sources mixing, we calculated a total sediment flux for the Var sediment routing system of 3.7 Mt/yr for the LGM. This corresponds to a specific sediment yield exceeding 1300 t/km²/yr. Sediment yields larger than 1000 t/km²/yr are commonly observed in small (< 10.000 km²) mountainous rivers located in active tectonic and extremely wet climate settings (i.e. Asia and Oceania; Milliman and Syvitski, 1992), but are also reported in (formerly) glaciated catchment (Church and Ryder, 1972; Hallet et al., 1996, Elverhøi et al, 1998). When compared with the modern Var sediment flux (1.63 Mt/yr; specific flux 580 t/km²/yr; Mulder et al., 1997), this indicates that sediment fluxes could have been higher by a factor 2.5 during the LGM because of glaciers. These results show that the fluvial erosion did not counterbalance the glacial erosion rate during glacial-interglacial cycles, thus confirming that the magnitudes of glacial-interglacial changes reported in many non-glaciated catchments (Hidy et al., 2014; Von Blanckenburg et al. 2015) are generally lower than those observed in glaciated ones (Church and Ryder, 1972; Elverhøi et al, 1998; Hinderer, 2001; Savi et al., 2014).

6.3. Similarities and differences in sediment flux reaction to the deglaciation in Western Europe basins.

The timing of post-LGM glacier retreat reported here for the Var system is consistent with that for the European ice sheet (Toucanne et al., 2015; Hughes et al., 2016; Fig. 4) even though small temperate glaciers might have been more sensitive to climate forcings than large ice caps (Jaeger et al., 2016). Based on this synchronization, the trend observed for the glacial-interglacial sediment supply in the Var system is compared with those determined in the alpine foreland (Hinderer et al., 2001) and off the Channel River system (Toucanne et al., 2010, 2015; Fig. 5), each of them being connected to ice caps during the last glacial period (Fig.1).

Since the paraglacial cycle was first described by Church and Ryder (1972) only a few studies have assessed the evolution of sediment export through glacial-interglacial periods whether in magnitude or timing (e.g. Elverhøi et al., 1998; Hinderer, 2001, 2012; Ballantyne, 2002; Savi et al., 2014) mainly because of the non-continuity of continental sequences and the difficulties in their dating. Conceptual models predict that sediment yield could be delayed with respect to sediment production, the time-lag depending on the size of the catchment area, the storage and release of sediments and the adaptation of fluvial systems (Church and Ryder, 1972; Harbor et Warburton, 1993; Ballantyne, 2002). Recently, Toucanne et al. (2015) demonstrated the synchronous occurrence of European ice-sheet withdrawal in the Northern European Lowlands and peaks in sediment fluxes off the Channel River, 2000 km downstream (Figs. 1, 4 and 5). This indicates that, at the scale of a large sediment routing system, only extreme meltwater flows can trigger the export of the glacigenic sediment produced throughout the last glacial especially during ice-sheet growth (Toucanne et al., 2015). A similar pattern is observed in the Rhone and Rhine catchments, with a pulse of sediment yield (exceeding the glacial 'norm' by a factor 3) during the deglaciation (Hinderer, 2001; see Lombo-Tombo et al., 2015 for an integrated view from the deep-sea). The sediment export pattern determined for the Var sedimentary system contrasts greatly with those define for the large-scale Rhine, Rhone and Channel River systems since the sediment flux in the Var system substantially decreased as soon as the glaciers retreated. This emphasizes the reactive character of the Var source-to-sink system, and confirms that the timing and duration for glacial sediment exhaustion are strongly dependent of the catchment's characteristics (Church and Ryder 1972; Harbor and Warburton, 1993; Ballantyne, 2002), with reduced-sized basins (i.e. here the Var River system) being more reactive than large ones because of higher slope, reduced delta and floodplain and more frequent large-magnitude sediment-transport events (Milliman and Syvitski, 1992; Covault et al., 2013). In contrast, in large-scale glaciated basins (i.e. Channel River system) sediment production greatly exceeds transport capacity, and the downstream release of sediments occurs mainly during deglacial phases, i.e. through meltwater pulses (Hinderer, 2001; Toucanne et al., 2010; 2015; Soulet et al., 2013). This explains why the post-glacial (paraglacial) landscape response (i.e. secondary sediment pulse) as observed in the Var sediment-routing system at ca. 11-9 ka, is often suspected but not clearly identified in larger systems (e.g. Erkens, 2009 and Hinderer, 2012 for the Rhine basin; Clift and Giosan, 2014 for the Indus basin).

7. Concluding remarks

The thorough analysis of continental and marine sediments collected along the Var sediment routing system (Southern French Alps - Western Mediterranean) gives new insights to our understanding of sediment production, transfer, and accumulation rates in natural systems. By focusing on the last glacial-interglacial transition, we demonstrated the substantial role of valley glaciers on the sediment budget, and their ability to synchronize the offshore sedimentary records to the onshore surface processes to ultimately produce a reactive sediment routing system. Importantly, our results confirm that glacier denudation rates tend to exceed fluvial rates over glacial-interglacial sediment flux cycle. The comparison of the proposed sediment export trend with those from large-scale Late Quaternary glaciated systems across Europe demonstrate the singularity of the Var river basin, and by extension the reactive character of small mountainous sediment routing systems. This highlights the importance of catchment's characteristics for the timing and duration of glacial sediment transfer from terrestrial source areas to deep-sea sinks. Recent evidence of glacier influence on sediment transfer at the scale of an entire sedimentary system should encourage further studies of deep-sea sediments to assess past glacier dynamics.

Acknowledgments

The authors acknowledge D. Vance, C. Pierre, R. Grischott, J. Woodward and an anonymous reviewer for their valuable comments and help to improve this article. We are grateful to Captain, Officers, crew members and principal investigator of the 2008 ESSDIV cruise onboard the R/V Pourquoi pas? for their technical support in recovering high-quality sediment piston cores. This project is funded by Université Pierre et Marie Curie (Institut des Sciences de la Terre de Paris), IFREMER (“Sedimentary Systems” and “Geological Hazards" research projects), the LabexMER (ANR-10-LABX-19-01) and the ECO-MIST project (#2010 JCJC 609 01). Authors specially thank J. Etoubleau, A. Roubi, M. Rovere, E. Ponzevera, N. Freslon and Y. Germain for their analytical support.

Figure Caption

Fig.1: Regional setting of the Var routing system. Geological map of the Var drainage area based on BRGM geological map 1:250 000 of Nice and Gap (Rouire et al., 1980 ; Kerckhove et al., 1979). The position of alpine glaciers at their LGM maximum extension is based on Julian (1977), Soutadé et al. (1987) and Buoncristiani and Campy (2004). For more details about the location of the core sites on the Var Sedimentary Ridge (VSR) refer to Bonneau et al. (2014). Note the absence of a continental shelf and the steepness of the continental slope off the Var River mouth. εNd was measured on the <63µm carbonate-free fraction of river sediments (report to Supplementary material for a detailed map). The upper right panel shows the paleogeography of western Europe showing the glacial limits of the European Ice Sheet (EIS) and the Alpine Ice Sheet (AIS) during the LGM (Ehlers et al., 2011). Locations of studied areas referred to in the discussion are also reported: Var River (this study), Channel River routing system (Toucanne, 2010; 2015), Alpine major valleys (Hinderer, 2001; Lombo-Tombo et al., 2015).

Fig. 2: Selected Harker's diagrams of major (CaO, Al_2O_3, K_2O, P_2O_5, TiO_2), Sr and LOI (Loss On Ignition) measured in river and turbidite samples (< 63 µm fraction). River sediments derived from erosion of the sedimentary formations are represented in blue, these samples were collected in the Esteron sub-basin (blue diamond), the upper part of the Var basin (blue cross), the Var lower valley (blue square) and in the SW part of the Tinée sub-basin (blue asterisk); river sediment derived from erosion of the External Crystalline Massifs are represented in red, these samples were collected in the Vésubie sub-basin (red triangle) and in the NE part of the Tinée sub-basin (red asterisk). Turbidite samples are represented by grey circles with the shade of grey indicating age (from 19 ka: dark grey to 15 ka: light grey,

see Table 1 for more details). Siliciclastic index: $(Al_2O_3+K_2O+Na_2O+TiO_2+MgO+Fe_2O_3)/(SiO2+CaO+Al_2O_3+K_2O+Na_2O+TiO_2+MgO+Fe_2O_3)$

Fig. 3: A. & B. Neodymium isotope composition (εNd) shown against Nd concentration (ppm) for river samples (Tinée sub-basin: red square; Vésubie sub-basin: yellow triangle; Esteron sub-basin and upper Var: Blue crosses; lower Var valley: green squares) and turbidite samples (black circles). Grey lines represent binary mixing curves between the three end-members for sediment sources in the drainage area (1) the Tinée Metamorphic Complex (TMC), (2) the sedimentary cover, and (3) the Oriental Metamorphic Complex (OMC), the interval between each points on the curve correspond to 10% in the binary mixing. In A.: fingerprints of the three end-members are given in Table 3. In B.: Nd concentration of end-members (1) and (3) are lowered to 30 ppm and a proportional relationship is imposed between end-member (1) and (3) allowing solution of the three end-members mixing model and calculate the contribution of each end-member in turbidite sediments (see main text for details). Mixing models presented in Table 4 are graphically represented in B. by three binary mixing curves (*c* and *b* for LGMl and *c* and *a* for Holocene). C. REE compositions of sediments normalized to Post-Archean average Australian Shale (PAAS; Taylor and McLennan, 1985).

Fig. 4: A. $\delta^{18}O$ *bulloides* record (red dots, Bonneau et al., 2014), lighter oxygen isotope ratios correspond to warmer and wetter climate (Interstadials 2 to 12), except during Heinrich stadials (HS) and 21st June insolation at 45°N (grey curve, Laskar et al. 2004). B. Vésubie River incision rates (Saillard et al. 2014). C. Evolution of εNd values of turbidite sediments (<63 μm; carbonate-free fraction) measured in ESSK08-CS01 (solid dots) and in ESSK08-CS13 (open dots). The εNd scale is converted to % of Oriental Metamorphic Complex (OMC)

in the sediment mixing of the carbonate-free fraction. Grey vertical bars underline periods of rapid change in continental sources inferred from εNd. D. Mean turbidite flux on VSR, vertical scale corresponds to fraction of maximum turbidite frequency averaged for the two cores (max frequency is $15.yr^{-1}$ in core ESSK08-CS13 and $47.yr^{-1}$ in core ESSK08-CS01). E. Probability distributions of alpine glacier advance and retreat ages (relative probability, unitless; note that the amplitude of probability only reflects the number of ages found, not the magnitude of events; see Supplementary material for more details). Data are compared with (F.) the turbidite flux recorded off the Channel River (Toucanne et al., 2015; note that the turbidite flux axis is on a log scale) and (G.) periods of high Channel River discharges interpreted as retreat of the southern Scandinavia Ice-Sheet (Toucanne et al., 2015).

Fig. 5: Schematic diagram of the deglacial evolution of sediment yield in the Var basin (A. Reactive basins) compared with large rivers (B. Buffered basins) connected to massive ice sheets: the Channel River (connected to Fennoscandian and British ice sheets; Toucanne et al., 2010, 2015) and rivers that drain the inner Alps (Hinderer, 2001). In these three areas, although deglaciation starts at ca. 20 ka and lasts no longer after 16 ka, the pattern of sediment excavation is different: for the small basin (Var) the peak of sediment yield is reached during the Last Glacial Maximum and gradually decreases during deglaciation, while for large basins (Channel River and inner Alps) the peak of sediment yield is reached during deglaciation coeval with a meltwater pulse (ie. when the transport capacity reached a maximum). A secondary pulse of sediment transport from formerly glaciated areas is observed in the Var system during the Early Holocene and is interpreted as a phase of reworking of glaciated sediments driven by the increase in rainfall as the interglacial climate set in.

Table Caption

Table 1: Chemical composition (% weight) of river and turbidite sediments. River samples are grouped by sub-basin; "Var upper valley" and "Var lower valley" refer to upstream and downstream from the Tinée confluence, respectively.

Table 2: Nd isotopic composition (εNd) and Nd concentration of <45 µm and 45-63 µm fractions of river samples (BV) turbidite sediment (ESSK08-CS01; cmbsf: centimeter below sea floor). The analytical error (2σ) on εNd is 0.2 units.

Table 3: Mean characteristics of the three main lithological units composing the Var catchment. Outcropping areas are normalized to the total drainage area (2830 km^2). The given mean εNd and Nd concentration are average values of <63 µm fraction of river sediments sampled downstream of outcropping areas.

Table 4: Estimated contributions of the three end-members in sediment flux. Note that the surface of drainage area did not change between Holocene and LGM. The Nd concentration of OMC and TMC end-members is lowered to 30 ppm for calculation (see text for details); data between brackets are estimated by using a Nd concentration of 50 ppm as observed in the catchment.

References

Adamson, K. R., J. C. Woodward, and P. D. Hughes (2014), Glaciers and rivers: Pleistocene uncoupling in a Mediterranean mountain karst, Quaternary Science Reviews, 94, 28-43.

Ballantyne, C. K. (2002), Paraglacial geomorphology, Quaternary Science Reviews, 21(18), 1935-2017.

Bayon, G., C. R. German, R. M. Boella, J. A. Milton, R. N. Taylor, and R. W. Nesbitt (2002), An improved method for extracting marine sediment fractions and its application to Sr and Nd isotopic analysis, Chemical Geology, 187(3–4), 179-199.

Bayon, G., J. A. Barrat, J. Etoubleau, M. Benoit, C. Bollinger, and S. Révillon (2009), Determination of Rare Earth Elements, Sc, Y, Zr, Ba, Hf and Th in Geological Samples by ICP-MS after Tm Addition and Alkaline Fusion, Geostandards and Geoanalytical Research, 33(1), 51-62.

Bayon, G., et al. (2015), Rare earth elements and neodymium isotopes in world river sediments revisited, Geochimica et Cosmochimica Acta, 170, 17-38.

Bigot-Cormier, F., R. Braucher, D. Bourlès, Y. Guglielmi, M. Dubar, and J. F. Stéphan (2005), Chronological constraints on processes leading to large active landslides, Earth and Planetary Science Letters, 235(1–2), 141-150.

Bonneau, L., S. J. Jorry, S. Toucanne, R. S. Jacinto, and L. Emmanuel (2014), Millennial-Scale Response of a Western Mediterranean River to Late Quaternary Climate Changes: A View from the Deep Sea, The Journal of Geology, 122(6), 687-703.

Bouchez, J., M. Lupker, J. Gaillardet, C. France-Lanord, and L. Maurice (2011), How important is it to integrate riverine suspended sediment chemical composition with depth? Clues from Amazon River depth-profiles, Geochimica et Cosmochimica Acta, 75(22), 6955-6970.

Buoncristiani, J.-F., and M. Campy (2004), The palaeogeography of the last two glacial episodes in France: The Alps and Jura, 101-110 pp., Elsevier, Amsterdam.

Calvès, G., et al. (2013), Inferring denudation variations from the sediment record; an example of the last glacial cycle record of the Golo Basin and watershed, East Corsica, western Mediterranean sea, Basin Research, 25(2), 197-218.

Carpentier, M., D. Weis, and C. Chauvel (2014), Fractionation of Sr and Hf isotopes by mineral sorting in Cascadia Basin terrigenous sediments, Chemical Geology, 382(0), 67-82.

Church, M., and J. M. Ryder (1972), Paraglacial Sedimentation: A Consideration of Fluvial Processes Conditioned by Glaciation, Geological Society of America Bulletin, 83(10), 3059-3072.

Clift, P. D., and L. Giosan (2014), Sediment fluxes and buffering in the post-glacial Indus Basin, Basin Research, 26(3), 369-386.

Clift, P. D., et al. (2008), Holocene erosion of the Lesser Himalaya triggered by intensified summer monsoon, Geology, 36(1), 79-82.

Cossart, E., M. Fort, D. Bourlès, R. Braucher, R. Perrier, and L. Siame (2012), Deglaciation pattern during the Lateglacial/Holocene transition in the southern French Alps. Chronological data and geographical reconstruction from the Clarée Valley (upper Durance catchment, southeastern France), Palaeogeography, Palaeoclimatology, Palaeoecology, 315, 109-123.

Covault, J., W. Craddock, B. Romans, A. Fildani, and M. Gosai (2013), Spatial and temporal variations in landscape evolution: Historic and longer-term sediment flux through global catchments, The Journal of Geology, 121(1), 35-56.

Darnault, R., Y. Rolland, R. Braucher, D. Bourlès, M. Revel, G. Sanchez, and S. Bouissou (2012), Timing of the last deglaciation revealed by receding glaciers at the Alpine-scale: impact on mountain geomorphology, Quaternary Science Reviews, 31(0), 127-142.

Ehlers, J., P. L. Gibbard, and P. D. Hughes (2011), Quaternary glaciations-extent and chronology: a closer look, Elsevier.

Elverhøi, A., R. L. Hooke, and A. Solheim (1998), Late Cenozoic erosion and sediment yield from the Svalbard–Barents Sea region: implications for understanding erosion of glacierized basins, Quaternary Science Reviews, 17(1-3), 209-241.

Erkens, G. (2009), Sediment dynamics in the Rhine catchment: quantification of fluvial response to climate change and human impact, Utrecht University.

Federici, P. R., A. Ribolini, and M. Spagnolo (2016), Glacial history of the Maritime Alps from the Last Glacial Maximum to the Little Ice Age, Geological Society, London, Special Publications, 433.

Gennesseaux, M. (1966), Prospection photographique des canyons sous-marins du Var et du Paillon (Alpes-Maritimes) au moyen de la Troïka, [s.n.], Paris.

Hallet, B., L. Hunter, and J. Bogen (1996), Rates of erosion and sediment evacuation by glaciers: A review of field data and their implications, Global and Planetary Change, 12(1–4), 213-235.

Harbor, J., and J. Warburton (1993), Relative rates of glacial and nonglacial erosion in alpine environments, Arctic and Alpine Research, 1-7.

Hidy, A. J., J. C. Gosse, M. D. Blum, and M. R. Gibling (2014), Glacial-interglacial variation in denudation rates from interior Texas, USA, established with cosmogenic nuclides, Earth and Planetary Science Letters, 390, 209-221.

Hinderer, M. (2001), Late Quaternary denudation of the Alps, valley and lake fillings and modern river loads, Geodinamica Acta, 14(4), 231-263.

Hinderer, M. (2012), From gullies to mountain belts: A review of sediment budgets at various scales, Sedimentary Geology, 280(0), 21-59.

Hughes, P., and J. Woodward (2009), Glacial and periglacial environments, The Physical Geography of the Mediterranean. Oxford University Press, Oxford, 353-383.

Hughes, A. L., R. Gyllencreutz, Ø. S. Lohne, J. Mangerud, and J. I. Svendsen (2016), The last Eurasian ice sheets–a chronological database and time-slice reconstruction, DATED-1, Boreas, 45(1), 1-45.

Ivy-Ochs, S., H. Kerschner, A. Reuther, F. Preusser, K. Heine, M. Maisch, P. W. Kubik, and C. Schlüchter (2008), Chronology of the last glacial cycle in the European Alps, Journal of Quaternary Science, 23(6-7), 559-573.

Jaeger, J. M., and M. N. Koppes (2016), The role of the cryosphere in source-to-sink systems, Earth-Science Reviews.

Jorry, S. J., I. Jégou, L. Emmanuel, R. Silva Jacinto, and B. Savoye (2011), Turbiditic levee deposition in response to climate changes: The Var Sedimentary Ridge (Ligurian Sea), Marine Geology, 279(1–4), 148-161.

Julian, M. (1977), Une carte géomorphologique des Alpes Maritimes franco-italiennes au 1/200 000e en couleurs. Présentation succincte, Méditerranée, 28(1), 45-53.

Kerckhove, C., and G. Monjuvent (1979), Carte geologique de la France à 1/250000, Feuille de Gap (35)Rep., BRGM.

Kettner, A. J., and J. P. M. Syvitski (2008), HydroTrend v.3.0: A climate-driven hydrological transport model that simulates discharge and sediment load leaving a river system, Computers & Geosciences, 34(10), 1170-1183.

Koppes, M. N., and D. R. Montgomery (2009), The relative efficacy of fluvial and glacial erosion over modern to orogenic timescales, Nat. Geosci., 2(9), 644-647.

Koppes, M., B. Hallet, E. Rignot, J. Mouginot, J. S. Wellner, and K. Boldt (2015), Observed latitudinal variations in erosion as a function of glacier dynamics, Nature, 526(7571), 100-103.

Laskar, J., P. Robutel, F. Joutel, M. Gastineau, A. Correia, and B. Levrard (2004), A long-term numerical solution for the insolation quantities of the Earth, Astronomy & Astrophysics, 428(1), 261-285.

Lombo-Tombo, S., B. Dennielou, S. Berné, M. A. Bassetti, S. Toucanne, S. J. Jorry, G. Jouet, and C. Fontanier (2015), Sea-level control on turbidite activity in the Rhone canyon and the upper fan during the Last Glacial Maximum and Early deglacial, Sedimentary Geology, 323, 148-166.

Marchandise, S., E. Robin, S. Ayrault, and M. Roy-Barman (2014), U-Th-REE-Hf bearing phases in Mediterranean Sea sediments: Implications for isotope systematics in the ocean, Geochimica Et Cosmochimica Acta, 131, 47-61.

Migeon, S., A. Cattaneo, V. Hassoun, C. Larroque, N. Corradi, F. Fanucci, A. Dano, B. M. De Lepinay, F. Sage, and C. Gorini (2011), Morphology, distribution and origin of recent submarine landslides of the Ligurian Margin (North-western Mediterranean): some insights into geohazard assessment, Marine Geophysical Research, 32(1-2), 225-243.

Milliman, J. D., and J. P. Syvitski (1992), Geomorphic/tectonic control of sediment discharge to the ocean: the importance of small mountainous rivers, The Journal of Geology, 525-544.

Molnar, P. (2004), Late Cenozoic increase in accumulation rates of terrestrial sediment: how might climate change have affected erosion rates?, Annu. Rev. Earth Planet. Sci., 32, 67-89.

Monegato, G., C. Ravazzi, M. Donegana, R. Pini, G. Calderoni, and L. Wick (2007), Evidence of a two-fold glacial advance during the last glacial maximum in the Tagliamento end moraine system (eastern Alps), Quaternary Research, 68(2), 284-302.

Mulder, T., and J. P. Syvitski (1995), Turbidity currents generated at river mouths during exceptional discharges to the world oceans, The Journal of Geology(103), 285-299.

Mulder, T., B. Savoye, J. P. M. Syvitski, and O. Parize (1997), Des courants de turbidité hyperpycnaux dans la tête du canyon du Var ? Données hydrologiques et observations de terrain, Elsevier, Paris, FRANCE.

Mulder, T., B. Savoye, D. J. W. Piper, and J. P. M. Syvitski (1998), The Var submarine sedimentary system: understanding Holocene sediment delivery processes and their importance to the geological record, Geological Society, London, Special Publications, 129(1), 145-166.

Piper, D. J. W., and B. Savoye (1993), Processes of late Quaternary turbidity current flow and deposition on the Var deep-sea fan, north-west Mediterranean Sea, Sedimentology, 40(3), 557-582.

Romans, B. W., S. Castelltort, J. A. Covault, A. Fildani, and J. P. Walsh (2015), Environmental signal propagation in sedimentary systems across timescales, Earth-Science Reviews.

Rouire, J., A. Autran, A. Prost, J. Rossi, and C. Rosset (1980), Carte géologique de la France à 1/250000, feuille de Nice (40)Rep., BRGM.

Saillard, M., C. Petit, Y. Rolland, R. Braucher, D. L. Bourlès, S. Zerathe, M. Revel, and A. Jourdon (2014), Late Quaternary incision rates in the Vésubie catchment area (Southern French Alps) from in situ-produced 36Cl cosmogenic nuclide dating: Tectonic and climatic implications, Journal of Geophysical Research: Earth Surface.

Sánchez Goñi, M., I. Cacho, J. Turon, J. Guiot, F. Sierro, J. Peypouquet, J. Grimalt, and N. Shackleton (2002), Synchroneity between marine and terrestrial responses to millennial scale climatic variability during the last glacial period in the Mediterranean region, Climate Dynamics, 19(1), 95-105.

Savi, S., K. P. Norton, V. Picotti, N. Akcar, R. Delunel, F. Brardinoni, P. Kubik, and F. Schlunegger (2014), Quantifying sediment supply at the end of the last glaciation: Dynamic reconstruction of an alpine debris-flow fan, Geological Society of America Bulletin, 126(5-6), 773-790.

Savoye, B., D. J. W. Piper, and L. Droz (1993), Plio-Pleistocene evolution of the Var deep-sea fan off the French Riviera, Marine and Petroleum Geology, 10(6), 550-571.

Simpson, G., and S. Castelltort (2012), Model shows that rivers transmit high-frequency climate cycles to the sedimentary record, Geology.

Soulet, G., G. Ménot, G. Bayon, F. Rostek, E. Ponzevera, S. Toucanne, G. Lericolais, and E. Bard (2013), Abrupt drainage cycles of the Fennoscandian Ice Sheet, Proceedings of the National Academy of Sciences, 110(17), 6682-6687.

Soutadé, G., M. Julian, J. Dresch, M. Chardon, and Y. Bravard (1987), Dynamique de l'évolution des reliefs au cours du Quaternaire, Méditerranée, 37-60.

Syvitski, J. P., and J. D. Milliman (2007), Geology, geography, and humans battle for dominance over the delivery of fluvial sediment to the coastal ocean, The Journal of Geology, 115(1), 1-19.

Taylor, S. R., and S. M. McLennan (1985), The continental crust: its composition and evolution. Blackwell Scientific Pub., Palo Alto, CA

Toucanne, S., G. Soulet, N. Freslon, R. Silva Jacinto, B. Dennielou, S. Zaragosi, F. Eynaud, J.-F. Bourillet, and G. Bayon (2015), Millennial-scale fluctuations of the European Ice Sheet at the end of the last glacial, and their potential impact on global climate, Quaternary Science Reviews, 123, 113-133.

Toucanne, S., S. Zaragosi, J.-F. Bourillet, V. Marieu, M. Cremer, M. Kageyama, B. Van Vliet-Lanoë, F. Eynaud, J.-L. Turon, and P. L. Gibbard (2010), The first estimation of Fleuve Manche palaeoriver discharge during the last deglaciation: Evidence for Fennoscandian ice sheet meltwater flow in the English Channel ca 20–18 ka ago, Earth and Planetary Science Letters, 290(3–4), 459-473.

Vescovi, E., C. Ravazzi, E. Arpenti, W. Finsinger, R. Pini, V. Valsecchi, L. Wick, B. Ammann, and W. Tinner (2007), Interactions between climate and vegetation during the Lateglacial period as recorded by lake and mire sediment archives in Northern Italy and Southern Switzerland, Quaternary Science Reviews, 26(11), 1650-1669.

Willenbring, J. K., A. T. Codilean, and B. McElroy (2013), Earth is (mostly) flat: Apportionment of the flux of continental sediment over millennial time scales, Geology.

Woodward, J. C., J. Lewin, and M. G. MacKlin (1992), Alluvial sediment sources in a glaciated catchment: The voidomatis basin, Northwest Greece, Earth Surface Processes and Landforms, 17(3), 205-216.

Woodward, J. C., R. H. B. Hamlin, M. G. Macklin, P. D. Hughes, and J. Lewin (2008), Glacial activity and catchment dynamics in northwest Greece: Long-term river behaviour and the slackwater sediment record for the last glacial to interglacial transition, Geomorphology, 101(1–2), 44-67.

Figure 1
Click here to download Figure: Figure 1.eps

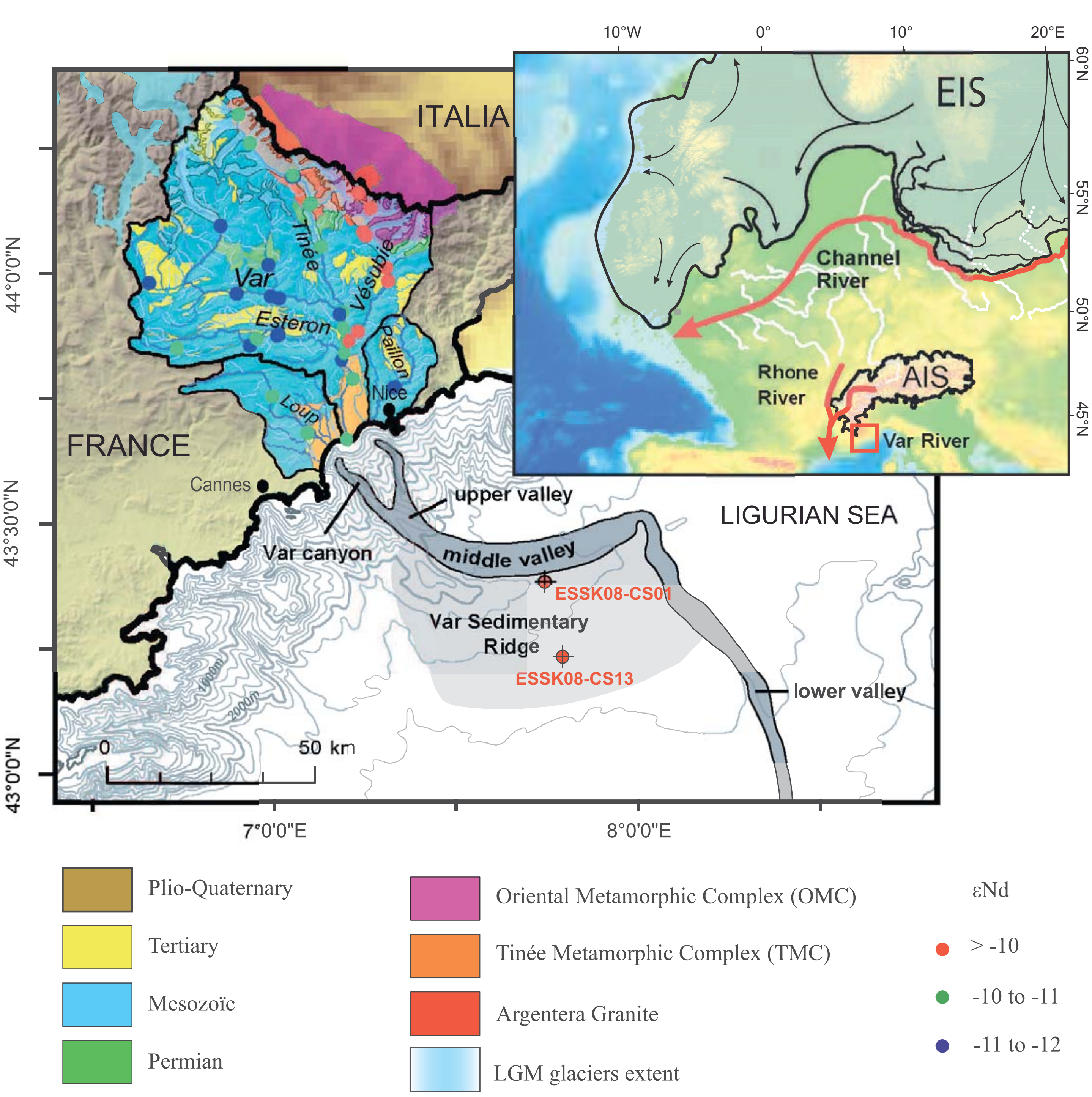

Figure 2

Click here to download Figure: Figure 2.eps

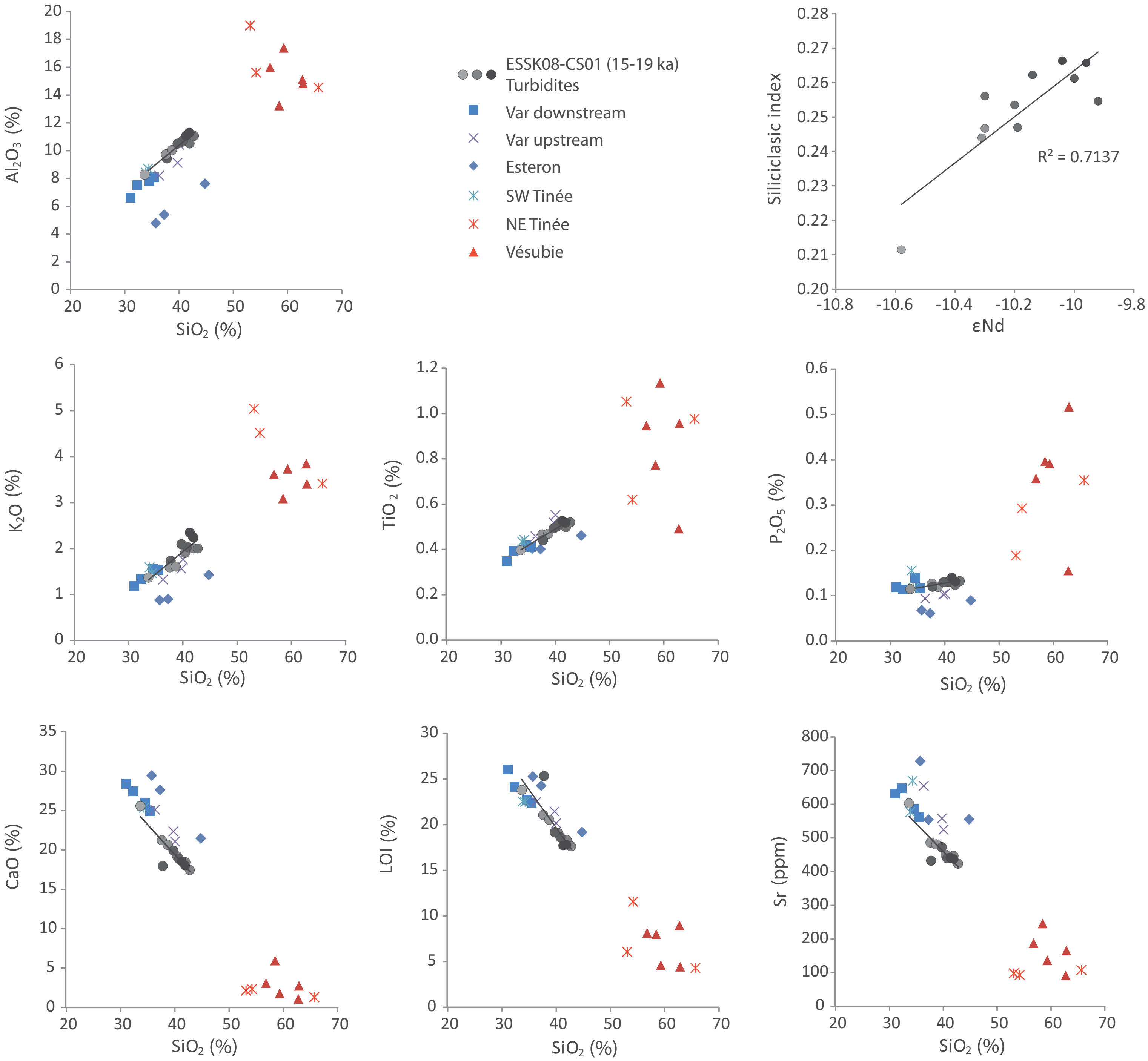

Figure 3

Click here to download Figure: Figure 3-review.eps

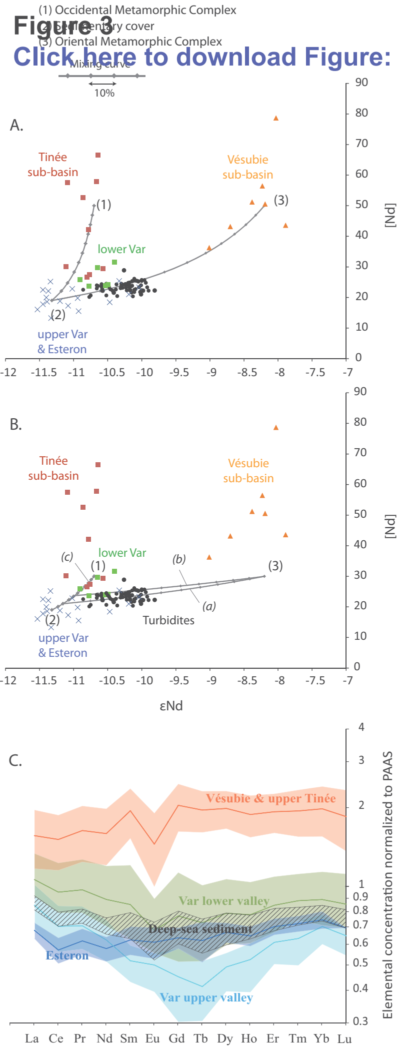

Figure 4

Click here to download Figure: Figure 4.eps

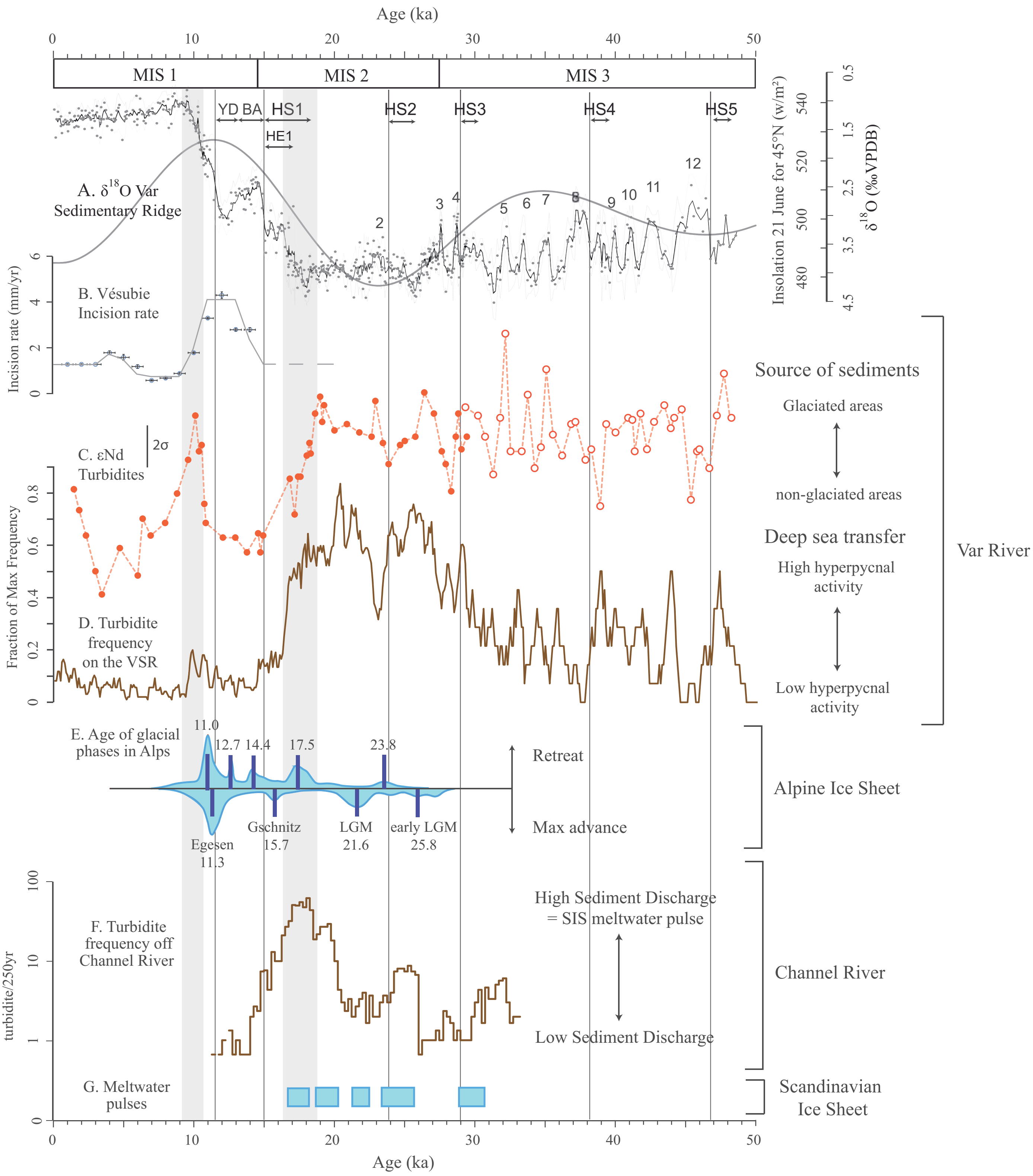

Figure 5
Click here to download Figure: Figure 5.eps

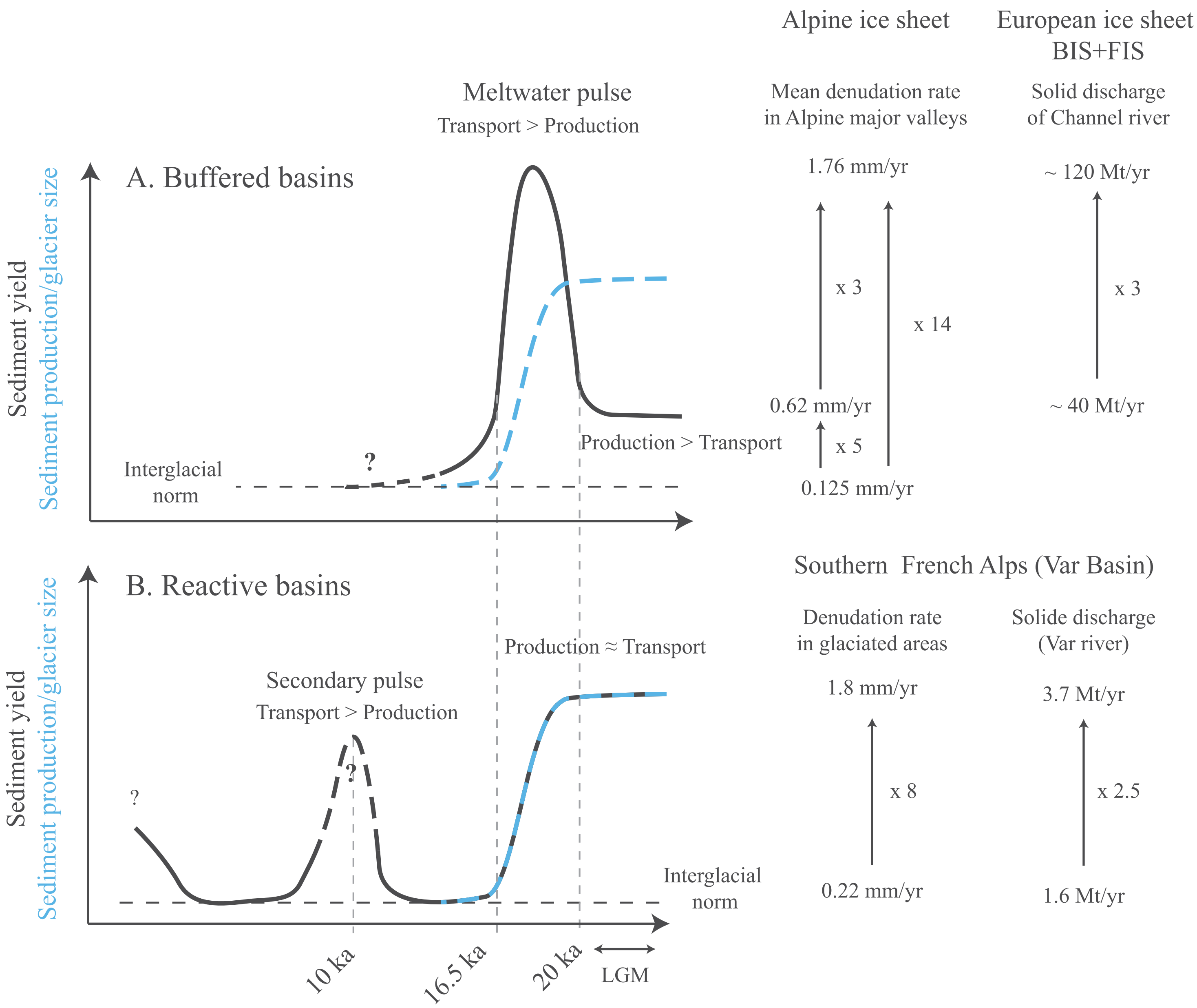

Table 1
Click here to download Table: Table1.docx

Table 1

Basin/Core	Sample /Depth in core (cm)	Long./ Age (ka)	Lat.	LOI (%)	SiO_2 (%)	Al_2O_3 (%)	Fe_2O_3 (%)	MnO (%)	CaO (%)	MgO (%)	K_2O (%)	Na_2O (%)	TiO_2 (%)	P_2O_5 (%)	SO_4 (%)	Sr (ppm)	Zr (ppm)
	BV-EST-04	*6.932*	*43.853*	24.3	37.3	5.4	2.0	0.01	27.6	0.8	0.89	0.14	0.40	0.06	0.59	554	131
Esteron	*BV-RIO-01*	*6.950*	*43.867*	19.2	44.8	7.6	2.5	0.02	21.5	1.2	1.42	0.66	0.46	0.09	0.38	555	144
	BV-RIOU-01	*7.010*	*43.875*	25.3	35.7	4.8	1.9	0.01	29.4	0.9	0.87	0.14	0.40	0.07	0.55	729	182
	BV-GUA-01	*7.311*	*44.002*	11.6	54.2	15.6	4.8	0.10	2.3	3.9	4.51	1.53	0.62	0.29	0.13	93	198
	BV-GUE-01	*7.054*	*44.185*	6.1	53.1	19.0	8.1	0.10	2.2	3.8	5.04	1.45	1.05	0.19	0.05	98	121
Tinée	*BV-MOL-01*	*7.101*	*44.130*	4.3	65.7	14.5	5.1	0.08	1.3	1.9	3.41	2.11	0.98	0.35	0.02	107	877
	BV-TIN-03	*7.051*	*44.185*	22.5	33.9	8.4	3.5	0.05	25.6	2.1	1.59	0.64	0.43	0.15	0.64	577	309
	BV-TIN-04	*7.054*	*44.184*	22.5	34.3	8.7	3.8	0.05	25.3	1.8	1.46	0.46	0.44	0.12	0.56	670	148
	BV-NEG-01	*7.237*	*44.151*	9.0	62.8	15.1	3.7	0.11	1.1	0.8	3.84	2.79	0.49	0.15	0.00	91	328
	BV-VES-01	*7.199*	*43.860*	8.0	58.5	13.2	4.0	0.06	5.9	2.9	3.08	2.23	0.77	0.40	0.29	246	624
Vésubie	*BV-VES-02*	*7.310*	*44.003*	4.4	62.9	14.8	4.5	0.08	2.7	2.3	3.40	2.51	0.96	0.52	0.11	165	2327
	BV-VES-03	*7.256*	*44.066*	4.6	59.3	17.4	6.1	0.10	1.8	2.4	3.73	2.40	1.14	0.39	0.02	136	846
	BV-VES-04	*7.315*	*43.976*	8.1	56.8	16.0	5.5	0.08	3.1	2.8	3.61	2.09	0.95	0.36	0.11	187	665
Var upper valley	*BV-VAR-01*	*7.191*	*43.837*	20.2	40.0	10.4	3.4	0.03	21.1	1.5	1.76	0.42	0.55	0.10	0.26	525	111
	BV-VAR-03	*6.896*	*43.955*	21.4	39.7	9.1	3.0	0.02	22.3	1.4	1.56	0.27	0.52	0.10	0.26	558	155
	BV-VAR-04	*7.012*	*43.946*	22.5	36.4	8.2	3.1	0.03	25.1	1.4	1.32	0.36	0.46	0.09	0.60	655	116
	BV-VAR-02	*7.191*	*43.837*	24.2	32.3	7.5	3.3	0.03	27.4	1.7	1.33	0.48	0.39	0.11	0.61	648	199
Var lower valley	*BV-VAR-05*	*7.198*	*43.861*	22.8	34.6	7.8	3.2	0.04	26.0	1.9	1.55	0.59	0.42	0.14	0.66	586	257
	BV-VAR-06	*7.197*	*43.667*	22.4	35.5	8.1	3.4	0.05	24.9	1.9	1.54	0.54	0.41	0.12	0.47	562	136
	BV-VAR-07	*7.197*	*43.667*	26.1	31.1	6.6	2.8	0.02	28.4	1.7	1.18	0.59	0.35	0.12	0.65	631	243
ESSK08-CS01	*543.5*	*15.9*		23.8	33.6	8.3	2.9	0.04	25.6	2.0	1.36	0.88	0.40	0.11	0.27	603	106
ESSK08-CS01	*573.5*	*16.9*		21.1	37.6	9.7	3.6	0.05	21.2	2.5	1.59	1.18	0.47	0.13	0.26	486	114
ESSK08-CS01	*617.5*	*17.5*		20.5	38.7	10.0	3.6	0.06	20.6	2.5	1.61	1.24	0.47	0.12	0.21	481	121
ESSK08-CS01	*630.5*	*17.6*		19.1	40.4	10.6	3.8	0.06	19.2	2.5	1.90	1.25	0.50	0.13	0.20	451	125
ESSK08-CS01	*663.5*	*18.1*		18.3	42.0	10.5	3.8	0.06	18.4	2.4	2.00	1.31	0.50	0.13	0.18	437	136
ESSK08-CS01	*677.5*	*18.3*		17.6	42.8	11.1	3.9	0.06	17.4	2.5	2.00	1.37	0.52	0.13	0.21	423	135
ESSK08-CS01	*707.5*	*18.7*		18.6	40.8	10.7	4.0	0.06	18.8	2.5	2.03	1.37	0.51	0.13	0.17	439	126
ESSK08-CS01	*734.5*	*19.0*		19.2	39.8	10.5	3.7	0.05	19.9	2.5	2.09	1.11	0.49	0.13	0.17	473	136
ESSK08-CS01	*747.5*	*19.2*		17.8	41.9	11.3	4.0	0.05	18.0	2.6	2.24	1.14	0.52	0.12	0.13	446	124
ESSK08-CS01	*762.5*	*19.3*		17.7	41.3	11.1	4.1	0.06	18.5	2.4	2.34	1.19	0.53	0.14	0.13	441	128
			Error (2s)		**0.21**	**0.16**	**0.13**	**0.011**	**0.1**	**0.13**	**0.025**	**0.063**	**0.012**	**0.015**	**0.028**	**6.6**	**3.7**

Table 2
Click here to download Table: Table 2.docx

Table 2

Sample/ Core	Longitude/ Depth in core (cmbsf)	Latitude/ Age (ka)	0-45 µm		45-63 µm		Sediment sources drained upstream
			εNd	[Nd] (ppm)	εNd	[Nd] (ppm)	
BV-EST-05	6.731	43.849	-11.2	21.9	-10.4	7.8	Multiple
BV-CIA-03	6.983	44.011	-10.8	25.9	-10.8	18.7	Single
BV-VAR-08	6.853	44.088	-11.2	23.2	-11.1	18.5	Single
BV-TIN-07	7.128	44.045	-10.7	35.7	-10.4	28.9	Multiple
BV-VAR-11	7.190	43.886	-10.9	25.1	-10.7	20.1	Multiple
BV-VAR-12	7.197	43.667	-10.3	23.7	-9.8	16.6	Multiple
BV-VES-05	7.231	43.878	-8.0	41.6	-7.9	43.0	Single
ESSK08-CS01	44.5	*1.5*	-10.6	23.3	-9.6	14.9	Multiple
ESSK08-CS01	197.5	*6.0*	-10.6	22.3	-10.1	11.4	Multiple
ESSK08-CS01	309.5	*8.9*	-10.5	23.3	-10.0	18.8	Multiple
ESSK08-CS01	361.5	*10.2*	-10.2	22.9	-8.8	20.5	Multiple
ESSK08-CS01	417.5	*10.8*	-10.4	21.5	-9.7	13.3	Multiple
ESSK08-CS01	533.5	*14.6*	-10.6	21.3	-9.8	13.6	Multiple
ESSK08-CS01	617.5	*17.5*	-10.4	24.0	-9.7	23.6	Multiple
ESSK08-CS01	707.5	*18.7*	-10.3	26.8	-9.4	12.2	Multiple
ESSK08-CS01	747.5	*19.2*	-10.1	22.6	-9.3	13.7	Multiple

Table 3

	Area (km²)	Area (%)	εNd	Nd (ppm)
Oriental Metamorphic Complex	192 km²	7%	-8.2	54
Tinée Metamorphic Complex	256 km²	9%	-10.7	51
Sedimentary cover	2352 km²	84%	-11.3	20

Table 4

	εNd	Decarb. Fraction (%)	Oriental Metamorphic Complex (%)		Tinée Metamorphic Complex (%)		Sedimentary formations (%)		Sediment flux (Mt/yr)	Specific Sediment flux (t/km²/yr)	Glaciers	
			in decarb. fraction	in total	in decarb. fraction	in total	in decarb. fraction	in total			Area (km²) (% of total)	volume ($10^{11} m^3$)
Holocene	-10.6	54	13 (8)	7 (5)	17 (11)	9 (6)	70 (81)	84 (89)	1.64[b]	580	0	0
LGM	-10.0	59	29 (23)	17 (14)	39 (31)	23 (18)	32 (46)	60 (68)	3.8 (6.7)	1339 (2367)	500 (17 %)	1.6[c]

b. modern sediment flux from Mulder et al. (1997)

c. calculated with *Hydrotrend* (Kettner and Syvitski, 2008)